Planetary and Space Science 236 (2023) 105747

Contents lists available at ScienceDirect

Planetary and Space Science

journal homepage: www.elsevier.com/locate/pss

On structural properties of Comet 67/P dust particles collected in situ by ROSETTA/COSIMA from observations of electrical fragmentation

Klaus Hornung [a,*], Eva Maria Mellado [a], Oliver J. Stenzel [b], Yves Langevin [c], Sihane Merouane [b], Nicolas Fray [d], Henning Fischer [b], John Paquette [e], Donia Baklouti [c], Anais Bardyn [d,g], Cecile Engrand [f], Hervé Cottin [d], Laurent Thirkell [g], Christelle Briois [g], Jouni Rynö [h], Johan Silen [h], Rita Schulz [i], Sandra Siljeström [j], Harry Lehto [k], Kurt Varmuza [l], Andreas Koch [m], Jochen Kissel [b], Martin Hilchenbach [b]

[a] Universität der Bundeswehr München, LRT-7, 85577, Neubiberg, Germany
[b] Max-Planck-Institut für Sonnensystemforschung, Justus-von-Liebig-Weg 3, 37077, Göttingen, Germany
[c] Institut d'Astrophysique Spatiale, CNRS / Université Paris Sud, Bâtiment 121, 91405, Orsay, France
[d] Univ Paris Est Creteil and Université Paris Cité, CNRS, LISA, 94010, Créteil, France
[e] NASA Goddard Space Flight Center, 8800 Greenbelt Rd, Greenbelt, MD, 20771, USA
[f] Centre de Sciences Nucléaires et de Sciences de la Matière, Bat.104, 91405 Orsay-Campus, France
[g] Laboratoire de Physique et Chimie de l'Environnement et de l'Espace (LPC2E), UMR CNRS 7328, Université d'Orléans, 45071, Orléans, France
[h] Finnish Meteorological Institute, Climate Research, Erik Palmenin aukio 1, P.O.Box 503, 00101, Helsinki, Finland
[i] European Space Agency, Scientific Support Office, Keplerlaan 1, Postbus 299, 2200 AG, Noordwijk, the Netherlands
[j] Department of Methodology, Textiles and Medical Technology, RISE Research Institutes of Sweden, Stockholm, Sweden, Box 5607, 114 86, Stockholm, Sweden
[k] Tuorla Observatory, Department of Physics and Astronomy, University of Turku, Väisäläntie 20, 33 21500, Piikkiö, Finland
[l] Institute of Statistics and Mathematical Methods in Economics, Vienna University of Technology, Wiedner Hauptstrasse 7/105-6, 1040, Vienna, Austria
[m] Von Hoerner und Sulger GmbH, Schlossplatz 8, 68723, Schwetzingen, Germany

ARTICLE INFO

Keywords:
Cometary dust
Rosetta mission
Charging
Porous aggregates
Fragmentation
Accretion

ABSTRACT

During ESA's Rosetta science mission, the COSIMA instrument collected dust particles in the coma of Comet 67P/Churyumov-Gerasimenko during two years near the comet's nucleus. The largest particles are about 1 *mm* in size. The collection process involved a low velocity impact on porous gold-black surfaces, often resulting in breakup, from which information on structural properties has previously been derived (Langevin et al., 2016). However, some of the particles were collected with little damage, but fragmented due to charging during subsequent secondary ion mass spectrometry. This report shows that the details of this electrical fragmentation support the concept of the existence of stable units with sizes of tens of μm within the incoming cometary dust particles prior to collection, possibly representing remnants of the early accretion processes.

1. Introduction

When the COSIMA (Cometary Secondary Ion Mass Analyzer) instrument (Kissel et al., 2007) on the Rosetta spacecraft (Glassmeier et al., 2007) began collecting cometary dust particles, it was soon observed that many of them broke up upon impact with the $10\,x\,10\,mm$ targets (Schulz et al., 2015), even though the arrival velocities relative to the spacecraft were only a few m/s as measured by the GIADA instrument (Rotundi et al., 2015). However, a certain percentage were found to show little damage on impact or even appear compact (Langevin et al., 2016). In the images of the particles with little damage, one could recognize individual smaller units in the order of tens of μm, and the fragments of those particles that underwent fragmentation were of similar size (Hornung et al., 2016; Merouane et al., 2017). This led us to suspect that these units already exist in the incoming dust and are not destroyed by the impact, i.e. they have a certain mechanical stability of their own. To avoid confusion with the much smaller submicron grains, we chose a separate name for them, "elements". They were found to be relatively densely packed within the dust particle (volume filling between 0.4 and 0.6), but must themselves be porous aggregates of the

* Corresponding author.
E-mail address: klaus.hornung@unibw.de (K. Hornung).

https://doi.org/10.1016/j.pss.2023.105747
Received 28 February 2023; Received in revised form 16 June 2023; Accepted 8 July 2023
Available online 11 July 2023

submicron grains, as suggested by microscopic examination of the MIDAS instrument on board Rosetta (Bentley et al., 2016), such that the total porosity of the incoming dust can reach values greater than 90%. The COSIMA team also analyzed the reflective properties of the dust, which showed volume scattering in addition to surface reflection and was transparent on scales of $\approx 25\ \mu m$, again indicating high porosity (Langevin et al., 2017). During the late phase of the Rosetta mission, in April 2016, some experiments were performed to gain further access to the mechanical properties of the collected dust (Hilchenbach et al., 2017). These included mechanical crushing, and observations of structural changes and electrical fragmentation due to positive charging of the dust induced by the primary ion beam of COSIMA. A quantitative measure of the charging potential could then be extracted from asymmetries in the line shapes of the peaks in the negative ion mass spectra ($\approx 70 - 130\ V$; Hornung et al., 2020). The present paper uses the details of the electrical particle fragmentation to derive further clues about the elements that may have survived the accretion processes to the cometary matter.

2. The COSIMA instrument onboard the Rosetta spacecraft

The COSIMA instrument was one of 11 scientific instruments on the Rosetta orbiter. It was designed to collect and analyze cometary dust particles in the coma, which are ejected from the nucleus of the comet near the Sun. It analyzed these dust particles in two ways: **(1)** The chemical composition was characterized using a time-of-flight secondary ion mass spectrometer (TOF-SIMS). It measured positive and negative secondary ions produced after bombardment with a pulsed primary ion beam (pulse width about 5 ns, repetition rate 1500 pulses/sec) of isotopically pure positive In^{115} ions from a liquid metal ion source. The energy of the primary ions is 8 keV and the footprint of the beam on the sample is approximately $35\ x\ 50\ \mu m$ full width half maximum. Selected dust particles were scanned either in an XY matrix, along an X or Y line scan, or at single spots with a secondary ion sampling time of 5 min at each position. **(2)** The optical appearance was measured using the COSISCOPE subsystem, a microscope camera with a pixel size of 14 μm. However, a higher spatial resolution could be obtained by moving the target relative to the camera in X and Y directions by an amount equal to half the pixel size (the target position could be manipulated with an accuracy better than 1 μm). The result is a spatial resolution of about 10 μm ("subpixel imaging", Langevin et al., 2016). The present paper uses data from this subsystem. In the examples presented, the cometary dust particles were collected on gold plates covered with a thin layer of gold black of 10–30 μm thickness. These gold blacks are extremely porous aggregates (porosity $\approx$ 90%) of nanometer sized gold particles. They are deep black (albedo 1.8 ± 0.6 %; Langevin et al., 2017), which allows the identification of the trapped dust particles on the targets.

3. Observations of fragmentation

3.1. Previous observations of impact fragmentation

Fig. 1 shows examples of dust particles collected during the early phase of the mission (October 2014 to February 2015). The particles 3D0 Nick and 3D0 Kerttu are compact-looking particles that show the tens of μm substructure. In both cases, the impact appears to have caused no damage to these particles. 3D0 Cora is an example of a particle that fragmented into smaller pieces that stayed close together. In the case of 2CF Fred fragments are ejected over larger distances, but part of it (lower left) still seems to stick together. 3D0 Vincenzo is considered a rubble pile with ejection of fragments of tens of μm in size. The different types of impact breakup have been discussed in detail previously (Langevin et al., 2016) and have also been used to estimate the strength of the dust, which was found to be of the order of $10^3 Pa$ (Hornung et al., 2016). A note on naming conventions: For example, 3D0 Nick refers to a particle named Nick at target number 3D0. Unless otherwise noted, the illumination in the images of this paper is from the right side under grazing incidence between 3° and 6°, as seen from the left-facing shadows. For further details on the imaging method, see Langevin et al. (2016).

3.2. Observations of electrical fragmentation

Analysis of the impact fragmentation did not resolve the question of whether the different degrees of damage were due to varying impact velocities or to different strengths. For example, the particle 3D0 Nick mentioned above was apparently very weakly attached to the target, as it changed position several times during the months after collection, indicating that it may have arrived at a very low velocity. Therefore, it was an important observation that some of the particles classified as compact fragmented under the primary ion beam of the SIMS during the acquisition of negative ion mass spectra (Hilchenbach et al., 2017). In this mode, the extraction voltage is biased to accelerate negative ions toward the mass spectrometer, while accelerating positive ions and also the positively charged dust fragments toward the grounded target (see Fig. A1 of Appendix). In contrast, in the positive ion mode, not only the positive ions but also the positively charged dust fragments are accelerated toward the spectrometer, which means that fragments may move away from the target and be lost for observation. Therefore, the standard SIMS measurement cycle on a new dust particle starts with the negative mode and then the positive ion mode. Images are taken before and after the SIMS measurements. Although COSIMA has analyzed a large number of dust particles, there are only a few for which the effects of impact fragmentation and electrical fragmentation can be clearly separated and for which images are available before and after negative SIMS analysis. Finally, five examples were selected where this is the case (see Table A for image acquisition dates).

In all images we have marked the area hit by the ion beam with a

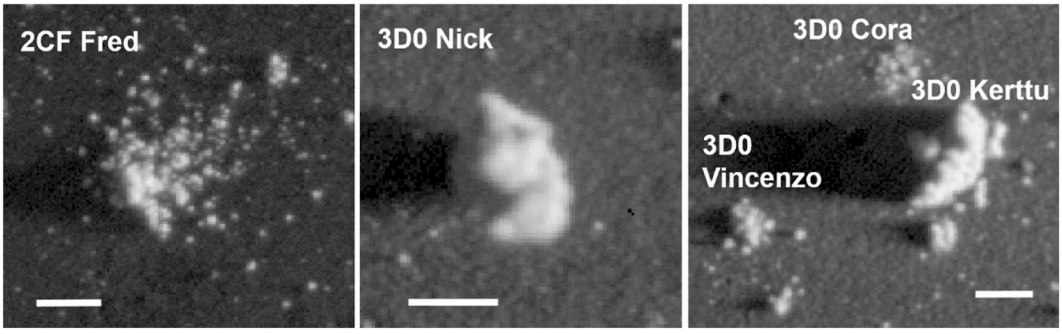

Fig. 1. Impact fragmentation: Examples of collected dust particles. Nick and Kerttu are compact looking particles. They do not show signs of fragmentation, unlike Fred, Cora and Vincenzo (scale bars: 200 μm; all are subpixel images).

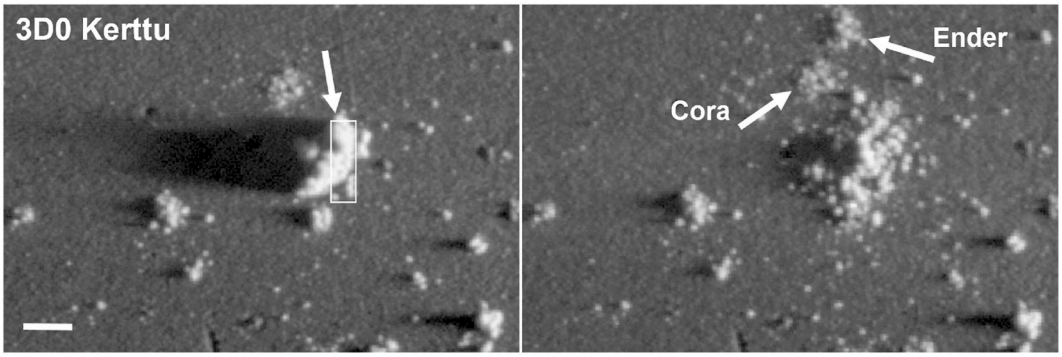

Fig. 2. Electrical fragmentation: Dust particle 3D0 Kerttu: before (left) and after (right) negative SIMS (scale bar: 200 μm). The arrow on the left image indicates the highest part of $\approx 150\ \mu m$, the white rectangle marks the area where the ion beam center hit the dust. Indication of jumping on the right image: The large fragment, 3D0 Kerttu-Ender, jumps over 3D0 Cora and fragments upon arrival at the target (see "fountain model" Sec. 4). Both images are with subpixel imaging.

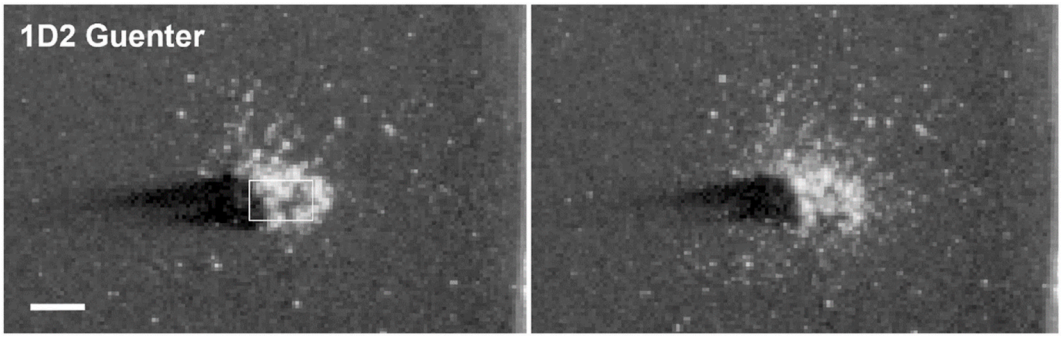

Fig. 3. Electrical fragmentation. Dust particle 1D2 Guenter: before (left) and after (right) negative SIMS (scale bar: 200 μm).

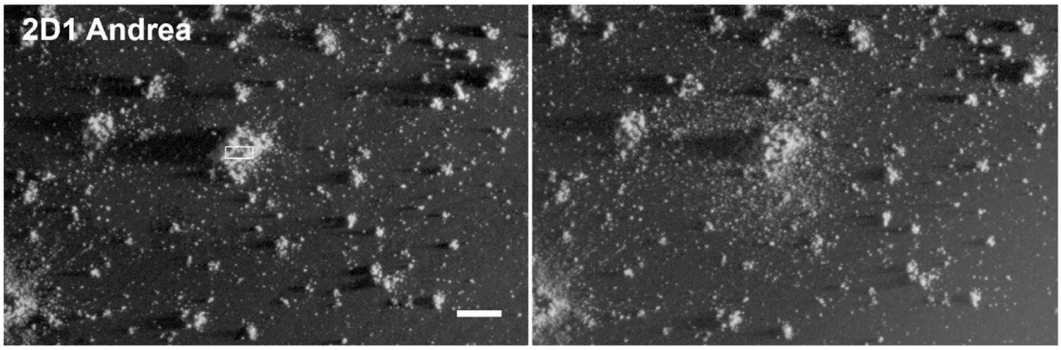

Fig. 4. Electrical fragmentation. Dust particle 2D1 Andrea: before (left) and after (right) negative SIMS (scale bar: 500 μm).

white rectangle. (1) Particle Kerttu (Fig. 2) had a very high part (about 150 μm, see arrow in left image) determined by a large shadow. Upon charging, the Kerttu core disintegrated into a pile of debris, and a very large fragment (Kerttu-Ender) was ejected finally fragmenting upon return to the target. (2) Particle 1D2 Guenter (Fig. 3) underwent substantial damage on impact and shows ejection of a cloud of small fragments. (3) Particle 2D1 Andrea (Fig. 4) is an example of a large particle that fragmented on impact and lost height on subsequent SIMS, accompanied by ejection of a large halo of fragments into the environment. (4) Particle 1D0 Andrzej (Fig. 5) was unaltered during collection and lost about 75% of its volume in the mechanical crushing experiment. The remaining part (shown in Fig. 5) did not change (Hilchenbach et al., 2017), but fragmented in the subsequent SIMS analysis, with the fragments spread over a larger area. The fragments are clearly distinguishable. (5) The particle 3D0 Hiroshi (Fig. 6), was also unaltered during collection. A subpixel image with enhanced resolution is available, taken shortly after collection, which shows the tens of μm granular structure and that the charging leads to disintegration, similar to the case of Andrzej. In this example, the area hit by the ion beam (white rectangle) is very narrow, but the whole particle is affected, indicating lateral charge transfer.

In summary, three main types of observations are made: **(1)** A granular agglomerate substructure with sub-unit sizes of tens of μm can be detected on the particles prior to their electrical fragmentation, and most of the fragments are in the same size range. This is particularly evident in the enhanced resolution images of Kerttu (Fig. 2), Andrzej (Fig. 5) and Hiroshi (Fig. 6). As noted above the same observation was made for impact fragmentation, where these sub-units were referred to as elements. Their re-appearance in the case of electrical fragmentation suggests that they represent stable units not only in the mechanical sense, but also in the electrical sense. **(2)** Inter-element rearrangements can be observed as a consequence of the charging, leading to a loss of

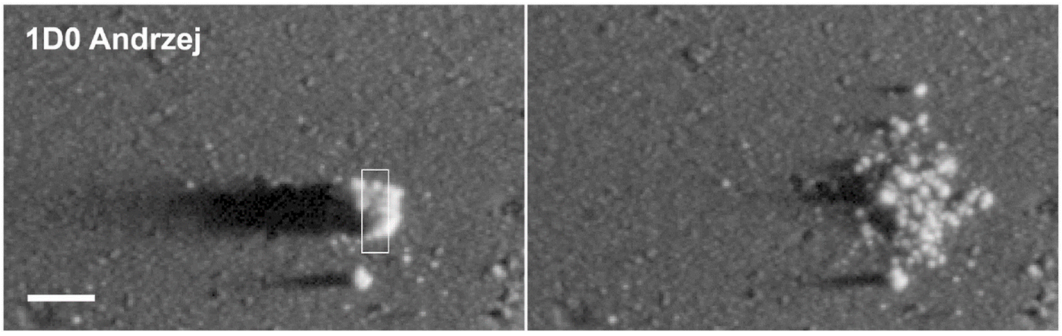

Fig. 5. Electrical fragmentation. Dust particle 1D0 Andrzej: before (left) and after (right) negative SIMS (scale bar: 200 μm). Both images with subpixel imaging.

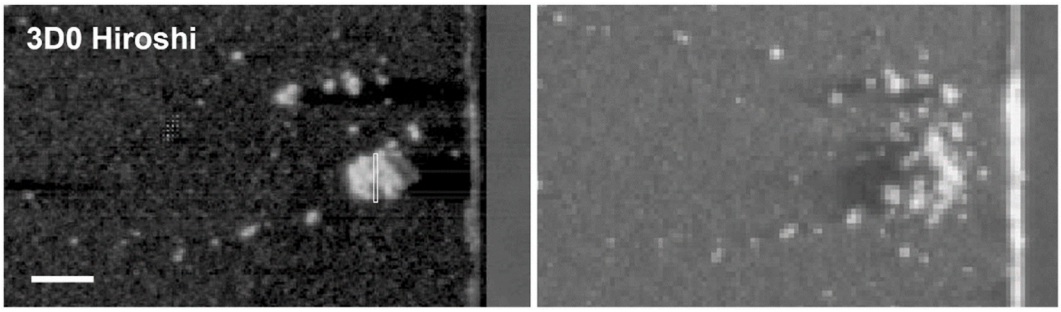

Fig. 6. Electrical fragmentation. Dust particle 3D0 Hiroshi: before (left) and after (right) negative SIMS (scale bar: 200 μm). Left image subpixel imaging (illumination from left), the granular structure is clearly visible.

height and a broadening of the base area (Kerttu, Fig. 2, Andrea, Fig. 4 and Guenter, Fig. 3). **(3)** Fragments, in most cases consisting of one or a few elements, are ejected into the environment. A theoretical understanding of these complex processes is difficult, especially the inter-element rearrangements. Numerical simulations can be helpful, as has been demonstrated in the case of impact fragmentation for a submicron model agglomerate substance (Lasue et al., 2019). However, one aspect can be treated in a simpler way, namely the distance that the ejected fragments travel before re-depositing on the target. It turns out that essential information can be derived from this parameter, leading to a consistent description within the elements concept.

3.3. Ejection distance and fragment size

The ejection distances are derived directly from the images taken immediately before and after exposure to the primary ion beam of the SIMS spectrometer (see Appendix A). Data reduction uses the DS9 software (Joye and Mandel, 2003) to detect changes between carefully aligned images. The results are shown in Fig. 7, where each fragment is represented by a circle indicating its size.

Particles Guenter and Andrea (Fig. 7a and b) have in common that two groups of ejected fragments can be observed. One group stays close to the remaining particle at distances of a few 100 μm. The rest is ejected over longer distances, up to a few mm. For Andrea, the close fragments are so numerous that they are indistinguishable on the images. The corresponding area has a triangular shape, represented by a dashed triangle in the plot. The number of ejected fragments in both examples is small compared to the remaining body of the particle. Particles Andrzej and Hiroshi (Fig. 7c and d) have in common that they are disintegrated entirely by the electric charging. The particle Kerttu (Fig. 7e) has the widest range of ejection distances of up to about 5000 μm. It represents a special case, as it was destabilized in a mechanical crushing test similar to that reported in Hilchenbach et al. (2017). A significant deformation is observed near the tip of the particle (see Fig. A2 in the Appendix). This could explain the ejection of the large fragment Kerttu-Ender, which traveled about 430 μm from its previous position. Since the space between Kerttu and Kerttu-Ender contains almost no fragments, as observed in Fig. 2, Kerttu-Ender must have jumped some distance and redeposited on the target. This observation is an important clue for understanding the electrical fragmentation process. Charged fragments, after being ejected from the parent dust particle, return to the target after a fountain-like parabolic flight in the extraction field of the spectrometer (see Fig. A1 of the Appendix).

In all examples, the size of the fragments is tens of μm Fig. 8 shows the size distribution of the fragments taken from all particles studied, except Kerttu due to its atypical history. The resulting power law exponent (3.3 $\pm$0.5) is close to the case of impact fragmentation (Merouane et al., 2017; Hornung et al., 2016). Averaging over multiple particles makes sense because the inter-element forces are of the van der Waals type, and the strength of these forces is insensitive to details of chemical composition (Israelachvili, 2011). The largest fragments ($d_{fr} \gtrsim$ 40 μm) appear in the images to be composed of multiple smaller elements, such that the size range of the element diameter (denoted " d") is narrow ($15 \lesssim d \lesssim 40$ μm), almost identical to that obtained from impact fragmentation.

There is no evidence that the charge produced by COSIMA's ion beam is breaking down the elements into smaller micron-sized units. If this were the case, there would be a very large number of small fragments, which would certainly be visible due to the high dynamic range of the pixel gray value amplitudes of our camera (up to a factor of 100 between the highest values on the dust and on the surrounding gold black). Their absence from the images suggests that if they are present, they represent a very small background. To find out what happens when finer dust is electrically fragmented, we performed laboratory tests with polydisperse SiO_2 dust particles composed of micron-sized monomers. They were shot at COSIMA targets at speeds of several m/s and their behavior on impact was studied (Ellerbroek et al., 2017, 2019). One of these targets was then introduced into the COSIMA laboratory model and a large particle was exposed to the SIMS primary ion beam.The resulting negative spectra indicate that it was charged to a potential of about 100 V. As a result, a fine white foggy area appeared, indicating the presence of micron-sized fragments, Fig. 9 (see also Hilchenbach, 2019).

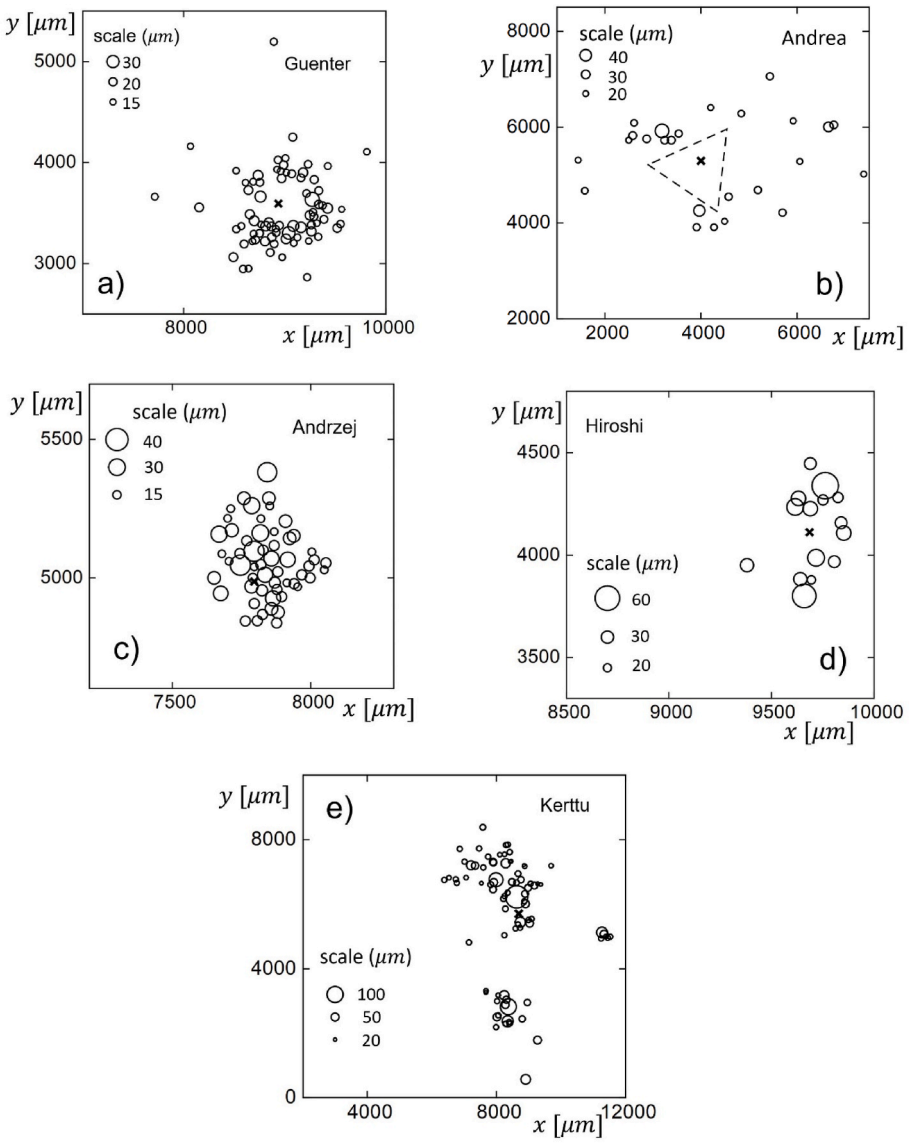

Fig. 7. Spatial distribution of fragments. The size of the circles indicates their equivalent spherical diameter, $d_{fr} = \left(\frac{6}{\pi} \cdot a_{fr} \cdot h_{fr} \cdot \varepsilon\right)^{1/3}$ where a_{fr} is the apparent area in the image plane, h_{fr} is the fragment height approximated by $h_{fr} \approx \sqrt{\frac{4}{\pi} \cdot a_{fr}}$ and ε is a parameter that describes the spatial shape of the fragment $\varepsilon \approx 0.5$ (an estimate between spherical: 2/3 and pyramidal: 1/3). The cross indicates the position of the particle's center before the electrical fragmentation.

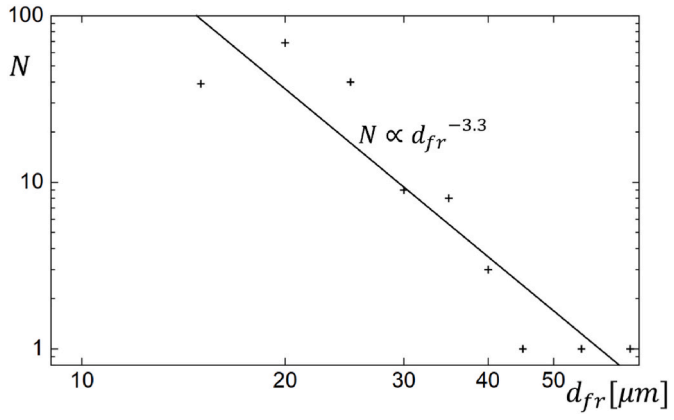

Fig. 8. Frequency size distribution of 171 fragments from the particles Guenter, Andrea, Andrzej and Hiroshi (N is the number of fragments within a binning interval of 5 μm, slope is -3.3 ± 0.5).

The disappearance of larger clumps of material further away from the SIMS area is not related to the ion beam charging, but caused by the extraction field alone (Kimura et al., 2020). In the case of the cometary dust collected by COSIMA, however, such "nebulae" are not observed (see e.g. Fig. 5). The elements remain intact during the electrical fragmentation process, and the space between the fragments is as black as in more distant empty sites. Thus, the conclusion is that the elements are the relevant "players" in the game of electrical fragmentation and that they are the ones carrying the charge. This also implies that their electrical conductivity must be greater than that of the dust particle as a whole. The reason is that the contact area between the elements is small, making conduction more difficult (the elements of 67/P dust were found to be insulators, but not the best ones; their specific resistivity was estimated to be $\approx 1.2 \cdot 10^{10}$ Ωm as a lower bound, Hornung et al., 2020). Additional evidence for the elements representing the charge carriers is discussed in the context of the dust's strength in Section 6.

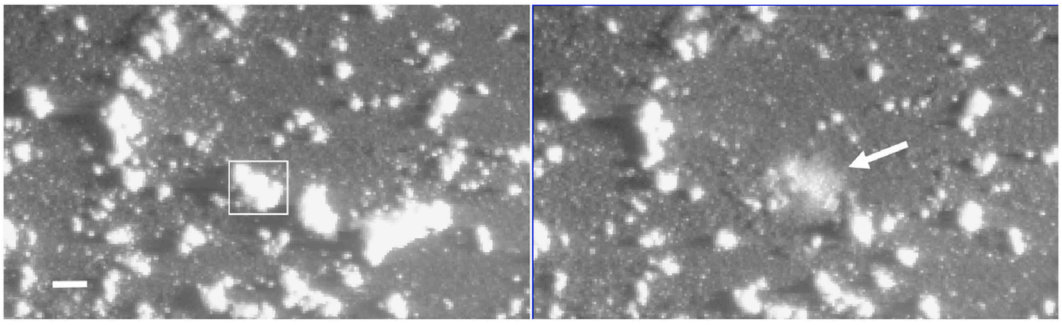

Fig. 9. COSIMA laboratory model: SiO_2 dust particles consisting of micron-sized monomers. Before (left) and after (right) SIMS analysis. The white rectangle indicates the SIMS area, the arrow indicates the "foggy" area consisting of fine fragments caused by negative mode SIMS (scale bar: 200 μm).

4. Theory: fountain model

The finding that the collected dust particles can be considered as agglomerates of the elements that are the relevant charge carriers opens the possibility of modelling the fragmentation process with the aim of understanding the observed fragment ejection distances from several 100 μm up to a few mm from the dust particle. For an approximate quantitative estimate, we consider the repulsive Coulomb potential energy stored in a system of n positively charged elements

$$\Phi(n) = \frac{1}{2} \cdot \sum_{i,j=1\ (i\neq j)}^{n} \frac{q_i q_j}{4\pi\varepsilon_0 \cdot |r_i - r_j|}, \tag{1}$$

as the energy released when all elements are moved to infinity from their positions r_i, r_j within the agglomerate (Brown and Hemingway, 1995). Here the vacuum permittivity ε_0 appears, since the relative permittivity is close to unity due to the high porosity of the dust ($\varepsilon_r < 1.2$; Hornung et al., 2020). Since the charging is limited to the area that is exposed to the primary ion beam, n is a small number. To further quantify Φ, we assume a system of spheres of equal diameter d and charge $q = 2\pi\varepsilon_0 \cdot d \cdot U$ that form three-dimensional aggregates of increasing number of elements n, where U is the sphere surface potential (equal diameters are assumed because the observed size range is narrow). Numerical tests showed that the exact spatial pattern of the aggregate is not critical as long as one excludes very elongated patterns (less than a factor of 2 in the ratio of the longest to the shortest dimension). Fig. 10 shows the results normalized to the binary case $n = 2$. Dense agglomerate clusters are a plane triangle ($n = 3$), a tetrahedron ($n = 4$) and a double-faced tetrahedron ($n = 5$). After that, simple cubic lattices with increasing number of elements were chosen. The reason for this choice is that simple cubic structures have almost the same volume filling of about 0.5 as the particles collected by COSIMA (Hornung et al., 2016). It should be noted, however, that this indicates the packing of the elements within the dust particle, the elements themselves having an internal porosity, so that the total porosity may well exceed 90%. When more than one configuration is possible for a given number n, the one with the smaller surface-to-volume ratio was chosen, since the observed fragments show little deviation from a symmetrical shape. To demonstrate the influence of different configurations, Fig. 10 contains two configurations for $n = 36$, the relatively compact $3 \times 3 \times 4$ and the more elongated $6 \times 3 \times 2$ lattice, showing that the difference is small. After normalization to the binary case, the results for $n > 4$ fit into a simple relationship: $\Phi(n)/\Phi(2) \approx a \cdot n^b$ with an asymptotic standard error of 6% for a and 1% for b (fitting range up to $n = 45$), while for the dense clusters $\Phi(n)/\Phi(2) = n \cdot (n-1)/2$ follows since for them the elements touch each other.

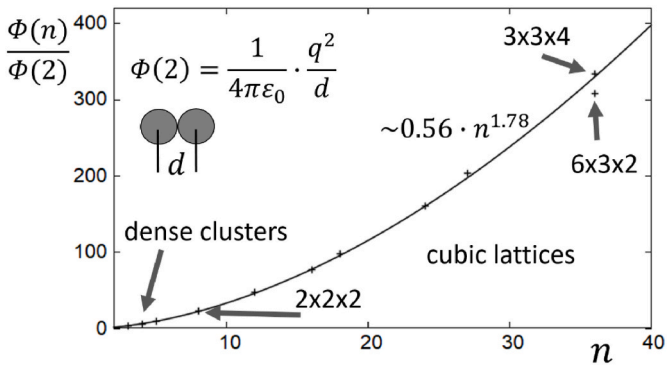

Fig. 10. Coulomb repulsive potential energy as a function of the number of charged elements in the agglomerate, normalized to the binary case.

Now consider a certain total number of elements n_{tot} charged within the ion beam footprint and the emission of a fragment containing n_{em} elements. Energy conservation shows that there is a certain amount of excess energy available for the kinetic energy of the emitted fragment:

$$\Delta\Phi(n_{tot}, n_{em}) = \Phi(n_{tot}) - (\Phi(n_{tot} - n_{em}) + \Phi(n_{em})), \tag{2}$$

where $\Phi(n_{tot})$ is the initial energy and $\Phi(n_{tot} - n_{em}) + \Phi(n_{em})$ is the final energy, if the interaction between the ejected fragment and the remaining agglomerate is negligible (which should be the case since the distance between the ejected fragment and the remaining agglomerate is much larger than the distance between the elements).

After emission at an angle α, the electric extraction field E_f applied between the grounded target and the secondary ion extraction lens of the spectrometer exerts a force on the positively charged fragment, accelerating it in a fountain-like parabolic trajectory toward the target until it lands at a distance l_h (see Fig. 11):

$$l_h(\alpha, h) = l_0 \cdot cos\ \alpha \cdot \left[sin\ \alpha + \sqrt{sin^2\ \alpha + \frac{2 \cdot h}{l_0}} \right], \tag{3}$$

where l_0 is the flight distance for zero launch height ($h = 0$) and an angle of $\alpha = 45$ degrees:

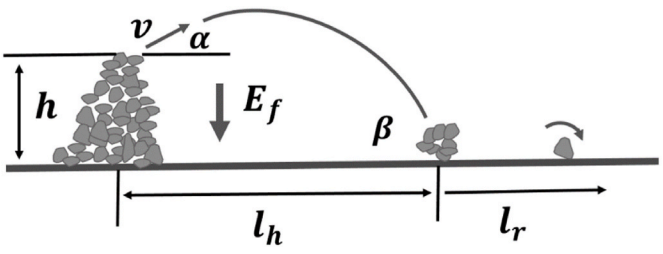

Fig. 11. Fountain-like ejection and subsequent rolling of fragments. l_h and l_r are the flight and rolling distances, respectively. E_f denotes the extraction field of the spectrometer. α is the emission angle and β is the impact angle at the target.

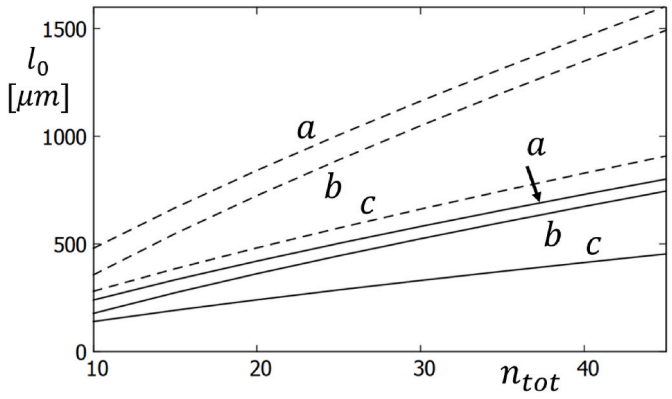

Fig. 12. Flight distance l_0 as a function of the total number of charged elements n_{tot} and the number of emitted elements n_{em}. a : $n_{em} = 1$; b: $n_{em} = 3$; c : case of complete disintegration into elements, $\Delta\Phi = \Phi(n_{tot})$. Solid lines: $U = 50V$, dashed lines $U = 100V$. The estimated value of n_{tot} for the COSIMA data is ≈ 25, as explained in the text.

$$l_0 = \psi(n_{tot}, n_{em}) \cdot \frac{U}{E_f} \quad \text{with} \quad \psi(n_{tot}, n_{em}) = \frac{\Delta\Phi(n_{tot}, n_{em}) / \Phi(2)}{n_{em}}. \tag{4}$$

U/E_f is a characteristic length ($\approx 83\ \mu m$ for $E_f = 1.2{\cdot}10^6\ V/m$, the fixed field value at the footprint of the primary ion beam and $U = 100\ V$ as an example). ψ is a dimensionless parameter that depends only on the element numbers involved, n_{tot} and n_{em}. To give an order of magnitude for l_0, Fig. 12 shows results for two values of the charging potential chosen to be in the order of the expected values. The curves a ($n_{em} = 1$) and b ($n_{em} = 3$) are derived from Eqs. (2) and (4) and curve c represents the case of complete disintegration which means that all n_{tot} elements are ejected (examples Andrzej and Hiroshi, see Section 3.3). In this case, Eq. (2) must be replaced by $\Delta\Phi = \Phi(n_{tot})$. An estimate for n_{tot} can be derived from the size of the primary ion beam ($\approx 35 \times 50\ \mu m$), which can touch about 4 elements, assuming an average size of $25\ \mu m$. In addition, there is evidence that the nearest neighbors are also charged due to lateral charge transfer, as can be seen in Fig. 6 (particle Hiroshi). This leads to values between 20 and 30 and we take as our nominal value $n_{tot} = 25 \pm 5$.

After landing on the target, the kinetic energy can be dissipated within the fragment if it consists of many elements (as in the example of the Kerttu-Ender fragment, Fig. 2). If it consists of only a few elements, as is the case for most fragments traveling longer distances, the kinetic energy is dissipated by rolling. In the case of impact fragmentation, rolling was the only possible displacement process of the fragments. Their typical rolling distances were of the order of several $100\ \mu m$, suggesting that the relevant forces between dust and target are of the van der Waals type. After adding the rolling contribution for the simplest case of a single element emitted, the total ejection distance becomes

$$l = l_h(\alpha, h) + l_r = l_h(\alpha, h) + \psi \cdot \frac{\pi\varepsilon_0 \cdot U^2}{2 \cdot C \cdot c_R}, \tag{5}$$

where C is the van der Waals interaction constant (Israelachvili, 2011), for which we use a numerical value of $\approx 2.6{\cdot}10^{-2} N/m$ from the previous study on impact fragmentation (Hornung et al., 2016). c_R is the coefficient of rolling friction, which for engineering systems has values between 0.1 (tires on sand) and 0.01 (tires on concrete, Bower, 2010). For our estimates, we exclude the smallest value because rolling is often associated with material loss, indicating a more intense interaction than simple rolling, and assume a value of 0.05, consistent with our findings for impact fragmentation. The total ejection distance becomes a maximum for an optimum emission angle of slightly less than 45°,

$$\alpha^{opt} = arctan\left({}^{1}/_{S}\right), \text{where } S(h, l_0) = \sqrt{1 + \frac{2h}{l_0}}, \tag{6}$$

corresponding to an impact angle at the target slightly greater than 45°, $\beta^{opt} = arctan\,(-S)$. Example model values for maximum ejection distances are listed in Table 1. It can be seen that the rolling contribution is significant and becomes dominant for charging potentials above 100 V.

It is interesting to note that since the process is purely electrical, neither the mass nor the size of the elements appear in Eq. (5). However, the size of the elements enters indirectly via the size of the ion beam footprint, which determines the n_{tot}. Other physical parameters require knowledge of size and density. For example, the emission velocity of the fragment is

$$v = v^* \cdot \sqrt{\psi(n_{tot}, n_{em})} \text{ where } v^* = \sqrt{\frac{12\varepsilon_0}{\rho}} \cdot \frac{U}{d}. \tag{7}$$

There is a slight size dependence of the density, which we previously estimated: $\rho \approx 5.25{\cdot}d^{-0.4}$ (ρ in kg/m^3 and d in m, Hornung et al., 2016) which leads to $v^* \approx \sqrt{2.29{\cdot}\varepsilon_0} \cdot \frac{U}{d^{0.8}}$. As an example, for $U = 100\ V$ and $d = 25{\cdot}10^{-6}\ m$, $v^* \approx 2.16\ m/s$ and for element numbers of $n_{tot} = 25$, $n_{em} = 3$ follows $\psi = 11$ and $v \approx 7\ m/s$.

5. Charging potentials from the ejection distances

Estimates for the charging potentials can be derived by inserting the maximum measured ejection distances (Fig. 7) into Eq. (5) with $\alpha = \alpha^{opt}$ and solving for U. The results are summarized in Table 2. For the height, the pre-fragmentation value h_1 is chosen. Since the farthest traveling fragments are single elements, the rolling contribution of Eq. (5) can be applied.

Kerttu shows the largest measured ejection distances of up to $5150\ \mu m$ leading to $U \approx 162\ V$. The large fragment Kerttu-Ender contains about 10 elements of nearly equal size of $20\ \mu m$ as seen in the

Table 1
Model maximum ejection distances from Eq. (5) and Eq. (6) for the example of emission of a single element, $n_{em} = 1$, $n_{tot} = 25$, $h = 100\ \mu m$. l_0: $\alpha = 45°$ flight distance for $h = 0$, $l_h{}^{max}$: maximum flight distance with h being $100\ \mu m$, l_r: rolling distance, l^{max}: total maximum ejection distance $l^{max} = l_h{}^{max} + l_r$, U: charging potential.

$U[V]$	$l_0[\mu m]$	$l_h{}^{max}[\mu m]$	$l_r[\mu m]$	$l^{max}[\mu m]$
50	503	595	323	918
100	1007	1102	1293	2395
150	1510	1607	2908	4516
200	2014	2111	5171	7282

Table 2
Observed values of maximum ejection distances l^{max} and pre- and post-fragmentation heights h_1 and h_2, respectively. Derived values of charging potential U, rolling distance l_r and electrical energy density $\sigma_{ed}{}^{el}$ (Section 6). Model parameters used are: ejection angle $\alpha = \alpha^{opt}$, rolling friction coefficient 0.05 and $n_{tot} = 25$. Kerttu[1)]: case of ejection of the big fragment Kerttu-Ender ($U = 53\ V$ represents a lower bound, see text).

Particle name	l^{max} $[\mu m]$	$h_1[\mu m]$	$h_2[\mu m]$	n_{em}	U $[V]$	$l_r[\mu m]$	$\sigma_{ed}{}^{el}[Pa]$
Kerttu	5150	150	56	1	162	3378	7691
Kerttu[1)]	430	150	56	10	53	–	1286
Guenter	1605	98	90	1	76	747	1693
Andrea	3400	180	130	1	124	1984	4506
Andrzej	400	100	50	25	37	102	401
Hiroshi	345	104	37	25	32	76	300

image. Its direction of ejection is not known. For Table 2, the optimum value of Eq. (6) is used, resulting in a potential of 53 V. This is a lower bound, since for any other angle higher potentials are required to produce the observed distance of Kerttu-Ender of 430 μm. No rolling is considered since the kinetic energy can be dissipated internally as suggested by the observed breakup upon re-impact on the target. The fragmentation patterns of Guenter and Andrea (Fig. 7 a,b) give interesting hints about the angular characteristics of their ejection. A significant fraction of the fragments stays close to the particle (about 500 – 600 μm) suggesting that their ejection is mainly in upward direction (α close to 90°), leading to short flight distances and an impact on the target approximately in normal direction ($\beta \approx 90$ degrees). In this case a part of the kinetic energy can be dissipated in the porous target material, leading to smaller rolling distances than those of Table 2, which are the relevant ones for the oblique impact angles close to 45°. A similar observation has been reported for another particle (1C3 Lou), where small fragments appeared as close as about 300 μm, although it was charged to about 90 V (Hilchenbach et al., 2017). There is a systematic experimental uncertainty with the Guenter particle. Its position is not far from the edge of the target at $x = 10\,000\ \mu m$ (Fig. 7a) and there is a possibility that larger ejections are not recorded because they do not settle within the target boundaries. Therefore its potential value may represent a lower limit. The fragmentation of particles Andrzej and Hiroshi is complete with no remaining body of the particle, and all the electrical energy stored in the n_{tot} charged elements is available for fragmentation. They show breakup at the lowest values, close to 30 V.

To estimate the accuracy of the derived potentials, the main input variables are the measured ejection distances, which have an uncertainty of less than 10%, the rolling force parameter $C{\cdot}c_R$, for which a value of about 20% is estimated, and n_{tot}, which is uncertain up to 20%. Using Eq. (5) for the error propagation within our model, the resulting total error for U is almost the same for all examples in Tables 2 and is close to 25%.

One can compare these potentials with those derived in our previous work on the asymmetries of the spectral mass lines (Hornung et al., 2020). However, one must be aware that the time scales of the processes involved are different. Charging and the onset of fragmentation occur in less than a few seconds (Hilchenbach et al., 2017), whereas the spectra acquisition time is 5 min for each position of the analyzing ion beam. Thus, the present values derived from fragmentation are transient, while those derived from spectral lines are steady state. The steady-state values range from 70 to 130 V, while the current values range from 30 to 162 V. Nevertheless, the approximate agreement between the two sets leads to the conclusion that steady-state potentials are reached quickly (of the order of seconds). Furthermore, the main hypothesis of the theoretical effort, which assumes a system of charged spherical elements of equal size and charge forming 3D aggregates, turns out to be realistic and leads to consistent results for the charging potentials.

6. A cross check with strength

The concept that the collected dust particles of Comet 67/P represent agglomerates of the elements is further confirmed when applied to the issue of strength. The situation is illustrated in Fig. 13.

The possibility that a dust particle of a few 100 μm is charged as a whole (Fig. 13 left) can be quickly ruled out. An estimate of the relevant Maxwell stress ($\sigma_M = 2 \cdot \varepsilon_0 \cdot \frac{U^2}{d^2}$) gives a value of only $\sigma_M \approx 3\ Pa$ for a charging potential of 100 V as an example, which is too low for breakup, since the strength of the dust is inferred to be in the order of $10^2 - 10^3\ Pa$. So the charge must be on smaller constituents of the agglomerate. For a quantitative estimate of the strength of an agglomerate to withstand electrical fragmentation, we use a breakup criterion analogous to mechanical impacts, where catastrophic breakup occurs when the kinetic energy density $\sigma_{ed} = \frac{\overline{\rho}}{2} \cdot v^2$ exceeds the strength of the material (v is the impact velocity and $\overline{\rho}$ the mean density of the impacting dust particle). Replacing the kinetic energy by the total electrostatic potential energy stored in the charged agglomerate of elements, as defined in Eq. (1), results in an "electric energy density":

$$\sigma_{ed}{}^{el} \approx \frac{\overline{\rho}}{\rho} \cdot 6 \cdot \varepsilon_0 \cdot \frac{U^2}{d^2} \cdot \frac{\Phi(n_{tot})}{\Phi(2) \cdot n_{tot}}, \tag{8}$$

where $\overline{\rho}, \rho$ are the mass densities of the dust agglomerate and its constituents, respectively (a typical value for $\frac{\overline{\rho}}{\rho}$ is about 0.5). If we assume that these constituents are the tens of μm sized elements and using a mean $n_{tot} \approx 25$, we obtain values of the order of $10^3 Pa$ for the example of Fig. 13, center, consistent with the result from impact fragmentation. If, on the other hand, the charged constituents are assumed to be the submicron grains (Fig. 13 right), then very high energy densities of the order of $10^7 Pa$ follow, or even higher if the number of charged elements also increases. This would be sufficient to pulverize the dust into very many submicron fragments, such as the "foggy areas" in our laboratory experiments with micron-sized SiO_2 dust, Fig. 9. However, this is not observed in the cometary dust collected by COSIMA.

Individual energy density values for the example particles are added to Table 2. They use the breakup potentials derived from the measured ejection distances and are therefore regarded as estimates for the strength. A mean element diameter of 25 μm is assumed (except for Kerttu-Ender where the data suggest a more specific value of 20 μm).

The lowest values of a few 100 Pa are for particles Hiroshi and Andrzej, which are least altered by the impact and can therefore be taken as best guesses for the strength of the incoming dust from the comet. Particles Guenter and Andrea were already deformed on impact, possibly leading to partial compaction and associated higher strength of several 1000 Pa (Blum et al., 2006). Particle Kerttu arrived at collection with little damage, but underwent damage during the mechanical pressing experiment on March 19, 2016 (see the image of Fig. A2 in the Appendix). One consequence is the ejection of the fragment Kerttu-Ender, which was apparently very loosely attached and was ejected at moderate energy density. A fragment of this size did not appear in any other breakup pattern, so it is very likely that it is connected to our crushing experiment. The other consequence is that the crushing caused a stronger compression of parts of Kerttu (the white circle in Fig. A2), leading to the observed highest ejection distances and a strength value close to 8000 Pa for the compressed part. The accuracy

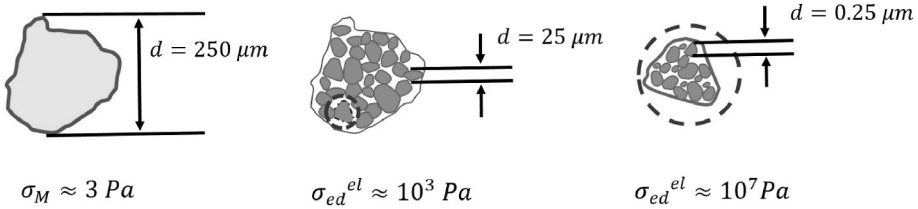

Fig. 13. Charge localization and electrical stresses for typical sizes. Left: Dust particle with charge continuously distributed throughout, center: The same particle but with charged units of tens of μm size (elements), right: magnified view of an element with submicron charged grains (example: charging potential $U = 100\ V$).

of the energy density values in Table 2 is estimated to be about ±40%, as derived from the uncertainties in the experimental data and model parameters (see Section 5). However, the model itself is an approximate one, so the strength information from the present experiments is expected to be accurate to within an order of magnitude.

Our strength considerations allow two conclusions: Agglomerate dry cometary coma dust particles may begin to become unstable to fragmentation into elements already at charging potentials as low as a few tens of volts. And second, the elements themselves do not fragment even at much higher potentials, as we could learn from those particles that were damaged at impact or during our crushing experiment.

7. Summary and conclusions

The concept of Comet 67/P dust particles as agglomerates of stable units, tens of μm in size (referred to as elements), initially inferred from the impact fragmentation at collection (Langevin et al., 2016; Hornung et al., 2016; Merouane et al., 2017), is independently confirmed by the present observations of electrical fragmentation. We studied a set of dust particles where we were sure to clearly separate the damages upon impact and charging. During SIMS ion bombardment, the dust particles are charged and disintegrate, their fragments scattering over the target and reaching distances of several $100-1000\ \mu m$. The fragment sizes were found to be almost identical to those of the impact fragments. Since the physical processes driving fragmentation by impact and charging are completely different, it is concluded that the fragment patterns reflect the internal structure of the dust rather than being a consequence of the fragmentation processes. By modelling the potential energy content of a system of charged elements, we were able to derive charging potentials from the measured flight distances of the fragments ($30 \lesssim U \lesssim 160\ V$) and found them to be consistent with values previously inferred from asymmetries in SIMS mass spectrum line shapes (Hornung et al., 2020). A discussion of the apparent strength of the dust further supports our structural concept. Larger dust particles of a few 100 μm are not charged as a unit, because the electric charge distributed over the entire particle would result in an electrostatic stress too low to induce the observed ejection. Instead, the charge must be distributed on the constituents, the elements. This leads to a second important conclusion, that the elements must have certain conductivity, but the dust agglomerate particles as a whole are less conductive. The strength of the dust particles to withstand electrical fragmentation into their elements could be inferred to be in the order of several $100-1000\ Pa$. None of our experiments resulted in breakup of the elements themselves, which means that their strength must be much greater than that for the agglomerate particles. Thus, the elements, intermediate in size between the submicron grains and the larger dust particles, are found to be both mechanically and electrically stable, having survived the several m/s impact upon collection as well as the relatively high charging voltages in the subsequent SIMS measurements.

The low strength of the dust agglomerate indicates that the binding forces holding the elements together are of the van der Waals type, while our data do not contribute to the properties at submicron scale, in particular to the question of how the grains are bound within the elements. This submicron fine structure of 67/P dust has been analyzed in detail by the MIDAS instrument on board Rosetta (Mannel et al., 2016, 2019; Bentley et al., 2016). They found that micron-sized particles have a porous hierarchical structure down to scales of tens of nanometers. Interestingly, they resemble the aggregates found in chondritic porous interplanetary dust particles, CP-IDPs, collected in the Earth's stratosphere, which are thought to originate from comets or asteroids. For example, the IDPs analyzed by Flynn et al. (2013) have sizes up to about 10 μm and high porosities between 0.7 and 0.94, close to the estimated internal porosities of our elements. They are found to resist fragmentation when charged by solar UV radiation, and the corresponding strength is estimated to be several 100 Pa as a lower bound, which the authors attribute to organic rims on the surface of smaller submicron constituents, possibly acting as a glue (see also Matrajt et al., 2012). Such organic matter could also contribute to the stability of the elements in our case, since in COSIMA dust particles the organic fraction was found to be about 45% of their mass (Bardyn et al., 2017; Fray et al., 2016). In general CP-IDPs are known to be rather heterogeneous at submicron scales, with a mixture of minerals and organics, crystalline and amorphous, and that different forms of binding contribute to their stability (Bradley, 2014; Engrand et al., 2016). In a recent review, Güttler et al. (2019) summarized the results for dust structural properties from the different Rosetta instruments. In their classification scheme, the dust particles discussed in the present work, as well as those studied by MIDAS, belong to the "porous group" and are best described as "agglomerate of agglomerates" (for a recent review on the issue of hierarchical agglomerate structures in cometary material, see Kimura et al., 2020).

Our findings are in line with an earlier theoretical prediction by Weidenschilling (1997) that units, tens of μm in size were formed in the early stages of the accretion process, and that they were subsequently assembled into larger structures during the formation of the protoplanetary disk (e.g. Dullemond and Dominik, 2005; Misener et al., 2019). The presence of stable units of the same size in the COSIMA collection suggests that the cometary material of 67/P is pristine in the sense that structures of the early accretion processes are still preserved. This imposes a constraint on subsequent processing steps, which must have been "soft" enough to leave these tens of μm units intact. For these subsequent steps, the present results may have an additional consequence. If accreted agglomerate dust particles can pick up charge (e.g., Ma et al., 2013; Flynn et al., 2013), then collisions between them could lead to a reverse process, electrical coagulation, in which the excess energy is absorbed rather than released, thereby increasing the likelihood of sticking. Finally, the field of light scattering is affected (e.g., Kolokolova et al., 2018), as the elements act as separate stable entities with their own electrical properties.

Declaration of competing interest

The authors declare that they have no known competing financial interests or personal relationships that could have appeared to influence the work reported in this paper.

Data availability

Data will be made available on request.

Acknowledgements

COSIMA was built by an international consortium of institutions led by the Max Planck Institute for Extraterrestrial Physics, Garching, Germany (for a detailed list see Kissel et al., 2007). We thank the Rosetta Science Ground Segment at ESAC, the Rosetta Mission Operations Center at ESOC, and the Rosetta Project at ESTEC for their outstanding work in enabling the scientific return of the Rosetta mission. One of the authors (K.H.) would like to thank Cornelius Schaumberger for valuable help in image analysis. The very constructive comments of the reviewers are gratefully acknowledged.

Appendix A. Schematic of the experimental setup and images used for analysis

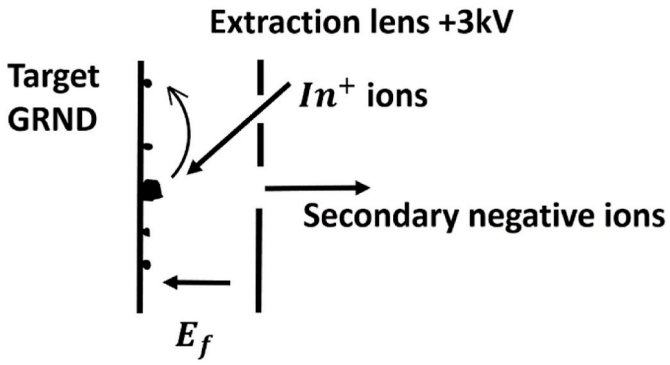

Fig. A1. Ejection of positively charged dust fragments in the spectrometer's extraction field E_f.

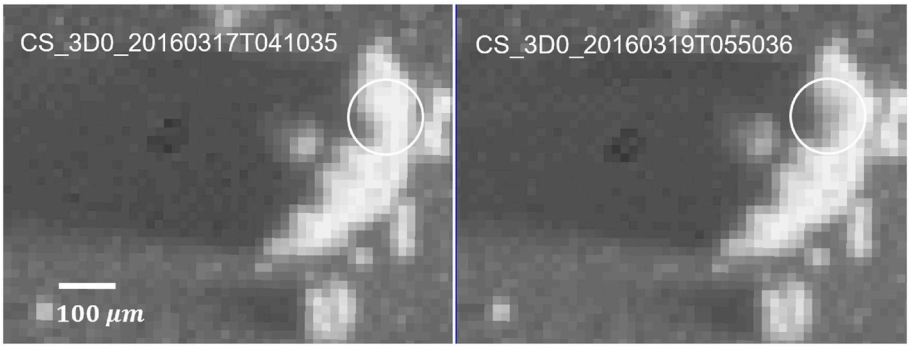

Fig. A2. Particle 3D0 Kerttu: Partial damage upon mechanical crushing on March 19, 2016. Left: before and right: after crushing.

For the analysis of the ejection distances, we used images immediately before and after the fragmentation event. Some of them are not identical to the images shown in the figures, because there we used resolution enhanced images whenever available to better visualize the situation, even if they were not immediately before or after. However, we have made sure that this choice does not introduce any artefacts. All images in this paper are logarithmically scaled due to the wide range of pixel gray value amplitudes, which are up to 100 times greater on a dust particle than on the black background.

Table A
Image Data. Note: In parentheses are those images in Fig. 1 through 6 that differ from the images used for the ejection distance analysis.

Particle name	Collection start	SIMS analysis start	Images before/after fragmentation
1D2 Guenter Jerisjarvi.1	2016_02_29	2016_04_14	2016_04_14/2016_04_15
2D1 Andrea Toisvesi.2	2015_05_11	2015_12_24	2015_12_24/2015_12_25 (2015_06_04/2015_12_25)
1D0 Andrzej Ukonvesi	2014_11_07	2016_04_20	2016_04_20/2016_04_20 (2016_04_13/2016_04_23)
3D0 Hiroshi Ukonvesi	2014_11_07	2016_05_04	2016_05_04/2016_05_04 (2014_12_14/2016_05_07)
3D0 Kerttu Rikkavesi	2014_10_18	2016_03_26	2016_03_25/2016_05_04 (2015_05_15/2016_05_04)
2CF Fred Kolima.3	2015_01_24	–	2015_02_10
3D0 Nick Ukonvesi	2014_11_07	–	2014_12_14
Laboratory data: SiO_2 on target No. 551	Ellerbroek et al. (2017)	2018_09_22	2018_09_21/2018_09_25

References

Bardyn, A., Baklouti, D., Cottin, H., et al., 2017. Carbon-rich dust in comet 67P/Churyumov-Gerasimenko measured by COSIMA/Rosetta. Mon. Not. Roy. Astron. Soc. 469, S712–S722. https://doi.org/10.1093/mnras/stx2640.

Bentley, M.S., Schmied, R., Thurid, M., et al., 2016. Aggregate dust particles at comet 67P/Churyumov–Gerasimenko. Nature 537, 73–75. https://doi.org/10.1038/nature19091.

Blum, J., Schräpler, R., Davidsson, B., Trigo-Rodriguez, J., 2006. The physics of protoplanetesimal dust agglomerates. I. Mechanical properties and relations to primitive bodies in the solar system. Astrophys. J. 652, 1768–1781. https://doi.org/10.1086/508017.

Bower, A.F., 2010. Applied Mechanics of Solids. C&C Press, Taylor and Francis, London, UK.

Bradley, J.P., 2014. Early Solar Nebula Grains – Interplanetary Dust Particles. Treatise on Geochemistry, second ed., vol. 1, pp. 287–308. https://doi.org/10.1016/B978-0-08-095975-7.00114-5 (Chapter 1).8.

Brown, R.C., Hemingway, M.A., 1995. Electric charge distribution and capacitance of agglomerates of spherical particles: theory and experimental simulation. J. Aerosol Sci. 26 (8), 1197–1206. https://doi.org/10.1016/0021-8502(95)00524-2.

Dullemond, C.P., Dominik, C., 2005. Dust coagulation in protoplanetary disks: a rapid depletion of small grains. A&A 434 (3), 971–986. https://doi.org/10.1051/0004–6361:20042080.

Ellerbroek, L.E., Gundlach, B., Landeck, A., et al., 2017. The footprint of cometary dust analogues – I. Laboratory experiments of low-velocity impacts and comparison with Rosetta data. Mon. Not. Roy. Astron. Soc. 469 (l_2), S204–S216. https://doi.org/10.1093/mnras/stx1257.

Ellerbroek, L.E., Gundlach, B., Landeck, A., et al., 2019. The footprint of cometary dust analogues – II. Morphology as a tracer of tensile strength and application to dust collection by the Rosetta Spacecraft. Mon. Not. Roy. Astron. Soc. 486, 3755–3765. https://doi.org/10.1093/mnras/stz1101.

Engrand, C., Duprat, J., Dartois, E., et al., 2016. Variations in cometary dust composition from Giotto to Rosetta, clues to their formation mechanisms. Mon. Not. Roy. Astron. Soc. 462 (l_1), S323–S330. https://doi.org/10.1093/mnras/stw2844.

Flynn, G.J., Wirick, S., Keller, P., 2013. Organic grain coatings in primitive interplanetary dust particles: implications for grain sticking in the Solar Nebula. Earth Planets Space 65, 1159–1166. https://doi.org/10.5047/eps.2013.05.007.

Fray, N., Bardyn, A., Cottin, H., et al., 2016. High-molecular-weight organic matter in the particles of comet 67P/Churyumov–Gerasimenko. Nature 538, 72–74. https://doi.org/10.1038/nature19320.

Glassmeier, K.-H., Boenhardt, H., Koschny, D., et al., 2007. The Rosetta mission: flying towards the origin of the solar system. Space Sci. Rev. 128, 1–21. https://doi.org/10.1007/s11214-006-9140-8.

Güttler, C., Mannel, T., Rotundi, A., et al., 2019. Synthesis of the morphological description of cometary dust at comet 67P/Churyumov-Gerasimenko. Astron. Astrophys. 630, A24. https://doi.org/10.1051/0004-6361/201834751.

Hilchenbach, M., Fischer, H., Langevin, Y., et al., 2017. Mechanical and electrostatic experiments with dust particles collected in the inner coma of comet 67P by COSIMA onboard Rosetta. Phil. Trans. R. Soc. A375, 20160255 https://doi.org/10.1098/rsta.2016.0255.

Hilchenbach, M., 2019. Cometary dust in-situ observations – next steps after Rosetta. EGU general assembly 2019. Geophys. Res. Abstr. 21, 2019–3334. EGU.

Hornung, K., Merouane, S., Hilchenbach, M., et al., 2016. A first assessment of the strength of cometary particles collected in-situ by the COSIMA instrument onboard ROSETTA. Planet. Space Sci. 133, 63–75. https://doi.org/10.1016/j.pss.2016.07.003.

Hornung, K., Mellado, E.M., Paquette, J., et al., 2020. Electrical properties of cometary dust particles derived from line shapes of TOF-SIMS spectra measured by the ROSETTA/COSIMA instrument. Planet. Space Sci. 182, 104758 https://doi.org/10.1016/j.pss.2019.104758.

Israelachvili, J.N., 2011. Intermolecular and Surface Forces, 3rd. edition. Academic Press.

Joye, W.A., Mandel, E., 2003. New features of SAOImage DS9. In: Payne, H.E., Jedrzejewski, R.I., Hook, R.N. (Eds.), Astronomical Data Analysis Software and Systems XII ASP Conference Series, Vol. 295, 2003, p. 489.

Kimura, H., Hilchenbach, M., Merouane, S., et al., 2020. The morphological, elastic, and electric properties of dust aggregates in comets: a close look at COSIMA/Rosetta's data on dust in comet 67P/Churyumov-Gerasimenko. Planet. Space Sci. 181, 104825 https://doi.org/10.1016/j.pss.2019.104825.

Kissel, J., Altwegg, K., Clark, B.C., et al., 2007. Cosima high resolution time-of-flight secondary ion mass spectrometer for the analysis of cometary dust particles onboard Rosetta. Space Sci. Rev. 128, 823–826. https://doi.org/10.1007/s11214-006-9083-0.

Kolokolova, L., Nagdimunov, L., Mackowski, D., 2018. Light scattering by hierarchical aggregates. J. Quant. Spectrosc. Radiat. Transfer 204, 138–143. https://doi.org/10.1016/j.jqsrt.2017.09.019.

Langevin, Y., Hilchenbach, M., Ligier, N., et al., 2016. Typology of dust particles collected by the COSIMA mass spectrometer in the inner coma of 67P/Churyumov Gerasimenko. Icarus 271, 76–97. https://doi.org/10.1016/j.icarus.2016.01.027.

Langevin, Y., Hilchenbach, M., Vincendon, M., et al., 2017. Optical properties of cometary particles collected by the COSIMA mass spectrometer on-board Rosetta during the rendezvous phase around comet 67P/Churyumov–Gerasimenko. Mon. Not. Roy. Astron. Soc. 469 (l_2), S535–S549. https://doi.org/10.1093/mnras/stx2070, 21 July 2017.

Lasue, J., Maroger, I., Botet, R., et al., 2019. Flattened loose particles from numerical simulations compared to particles collected by Rosetta. A&A 630, A28. https://doi.org/10.1051/0004-6361/201834766 (2019).

Ma, Q., Matthews, L.S., Land, V., Hyde, W., 2013. Charging of aggregate grains in astrophysical environments. Astrophys. J. 763, 77. https://doi.org/10.1088/0004-637X/763/2/77.

Matrajt, G., Messenger, S., Joswiak, D., 2012. Diverse forms of primordial organic matter identified in interplanetary dust particles. Meteorit. Planet. Sci. 47 (4), 525–549. https://doi.org/10.1111/j.1945-5100.2011.01310.x.

Mannel, T., Bentley, M.S., Schmied, R., et al., 2016. Fractal cometary dust – a window into the early Solar System. Mon. Not. Roy. Astron. Soc. 462, S304–S311. https://doi.org/10.1093/mnras/stw2898.

Mannel, T., Bentley, M.S., Boakes, P.D., et al., 2019. Dust of comet 67P/Churyumov-Gerasimenko collected by Rosetta/MIDAS: classification and extension to the nanometer scale. Astron. Astrophys. 630, A26. https://doi.org/10.1051/0004-6361/201834851.

Merouane, S., Stenzel, O., Hilchenbach, M., et al., 2017. Evolution of the physical properties of dust and cometary dust activity from 67P/Churyumov–Gerasimenko measured *in situ* by *Rosetta*/COSIMA. Mon. Not. Roy. Astron. Soc. 469 (l_2), S459–S474. https://doi.org/10.1093/mnras/stx2018, 21 July 2017.

Misener, W., Krijt, S., Ciesla, F.J., 2019. Tracking dust grains during transport and growth in protoplanetary disks. ApJ 885 (2), 118. https://doi.org/10.3847/1538-4357/ab4a13.

Rotundi, A., Sierks, H., Della Corte, V., et al., 2015. Dust measurements in the coma of comet 67P/Churyumov-Gerasimenko inbound to the Sun. Science 347 (6220), 3905. https://doi.org/10.1126/science.aaa.3905.

Schulz, R., Hilchenbach, M., Langevin, Y., et al., 2015. Comet 67P/Churyumov-Gerasimenko sheds dust coat accumulated over the past four years. Nature 518, 216–218. https://doi.org/10.1038/nature14159.

Weidenschilling, S.J., 1997. The origin of comets in the solar nebula: a unified model. Icarus 127, 290–306. https://doi.org/10.1006/icar.1997.5712.